Applied Physics Letters

RESEARCH ARTICLE | MAY 09 2024

Calculating the acoustic radiation force on spherical particles in a standing ultrasound wave field considering single and multiple scattering

Soheyl Noparast ; Fernando Guevara Vasquez ; Mathieu Francoeur ; Bart Raeymaekers

Check for updates

Appl. Phys. Lett. 124, 192204 (2024)
https://doi.org/10.1063/5.0207695

View Online
Export Citation

13 May 2024 21:11:51

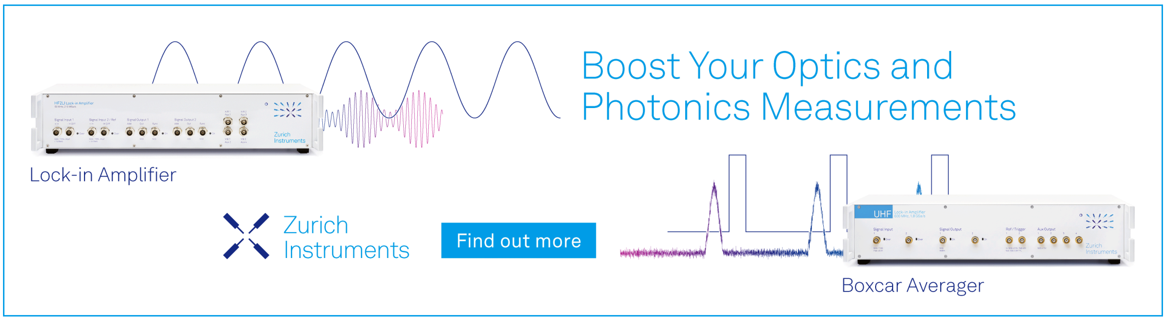

AIP Publishing

Calculating the acoustic radiation force on spherical particles in a standing ultrasound wave field considering single and multiple scattering

Cite as: Appl. Phys. Lett. **124**, 192204 (2024); doi: 10.1063/5.0207695
Submitted: 10 March 2024 · Accepted: 29 April 2024 ·
Published Online: 9 May 2024

View Online Export Citation CrossMark

Soheyl Noparast,[1] Fernando Guevara Vasquez,[2] Mathieu Francoeur,[3,4] and Bart Raeymaekers[1,a)]

AFFILIATIONS

[1]Department of Mechanical Engineering, Virginia Tech, Blacksburg, Virginia 24061, USA
[2]Department of Mathematics, University of Utah, Salt Lake City, Utah 84112, USA
[3]Department of Mechanical Engineering, McGill University, Montréal, Quebec H3A 0C3, Canada
[4]Department of Mechanical Engineering, University of Utah, Salt Lake City, Utah 84112, USA

[a)]Author to whom correspondence should be addressed: bart.raeymaekers@vt.edu

ABSTRACT

Ultrasound directed self-assembly (DSA) utilizes the acoustic radiation force (ARF) associated with a standing ultrasound wave to organize particles dispersed in a fluid medium into specific patterns. The ARF is a superposition of the primary acoustic radiation force, which results from the incident standing ultrasound wave, and the acoustic interaction force, which originates from single and multiple scattering between neighboring particles. In contrast with most reports in the literature that neglect multiple scattering when calculating the ARF, we demonstrate that the deviation between considering single or multiple scattering may reach up to 100%, depending on the ultrasound DSA process parameters and material properties. We evaluate a theoretical case with three spherical particles in a viscous medium and derive operating maps that quantify the deviation between both scattering approaches as a function of the ultrasound DSA process parameters. Then, we study a realistic system with hundreds of particles dispersed in a viscous medium, and show that the deviation between the ARF resulting from single and multiple scattering increases with decreasing particle size and increasing medium viscosity, density ratio, compressibility ratio, and particle volume fraction. This work provides a quantitative basis for determining whether to consider single or multiple scattering in ultrasound DSA simulations.

Published under an exclusive license by AIP Publishing. https://doi.org/10.1063/5.0207695

13 May 2024 21:11:51

Ultrasound directed self-assembly (DSA) utilizes the acoustic radiation force (ARF) associated with a standing ultrasound wave to organize and orient particles dispersed in a fluid medium into specific patterns.[1] The ARF derives from the acoustic radiation potential (ARP), and it drives spherical [2] or high aspect ratio particles[3] to the locations where the ARP is locally minimum and the ARF approaches zero.[4] Thus, ultrasound DSA finds application in a broad spectrum of engineering applications, such as non-contact manipulation of particles and objects,[5–8] levitated displays,[9,10] organizing and separating cells in lab-on-a-chip devices,[11] and manufacturing engineered composite materials that derive their tailored properties from the spatial organization of particles in the matrix material. The latter requires integrating ultrasound DSA with other manufacturing processes to create the material geometry, including formative processes such as mold casting[12–14] and freeze casting[15,16] or additive manufacturing (AM) such as direct ink writing (DIW)[17–20] and vat photopolymerization (VP).[21–25]

ARF is the superposition of the primary acoustic radiation force (PARF), which results from the incident standing ultrasound wave, and the acoustic interaction force (AIF), which originates from the acoustic interactions between neighboring particles.[26] Researchers have studied the acoustic interactions between spherical particles using single scattering (see, e.g., Refs. 26–31) and multiple scattering (see, e.g., Refs. 32–36) and several publications argue that the effect of multiple scattering on the ARF is small and can be neglected in favor of single scattering.[26,28,29,31] However, physically, it appears that multiple scattering becomes increasingly important with increasing particle volume fraction and local particle packing density, when particles are in close proximity and the acoustic interactions between them increase.[37]

Accurately calculating the ARF is essential when using ultrasound DSA in engineering applications. Consequently, several researchers have studied the effect of using different scattering approaches in ultrasound DSA simulations. Many research groups, including ours, have studied the effect of ultrasound DSA process parameters on the organization and orientation of particles in multiple dimensions in both inviscid and viscous media based only on the PARF, i.e., neglecting the AIF (e.g., spherical particles in 1D,[38,39] 2D,[7,40,41] and 3D,[42–44] high aspect ratio particles in 2D,[45–47] and 3D[48,49]). On the other hand, several researchers have also accounted for both the PARF and AIF using single scattering[26–31] and multiple scattering[32–36] and demonstrated that scattering of a plane ultrasound wave between spherical particles can either strengthen or weaken the ARF depending on their size and relative location and that single scattering dominates multiple scattering. Specifically, Silva and Bruus[26] theoretically demonstrated that the AIF between spherical particles in an inviscid medium subject to a plane ultrasound wave can be attractive or repulsive, accounting for single scattering only. Similarly, Lopes *et al.*[34] analyzed the AIF between spherical particles in an inviscid medium subject to a plane ultrasound wave, but accounted for multiple scattering, and determined that its effect on the AIF depends on the relative position of the particles.

The literature does not provide any comparison between the ARF that acts on spherical particles in a viscous medium when accounting for single or multiple scattering. However, this information is important to accurately simulate the locations where particles organize during ultrasound DSA. Hence, the objective of this work is to quantify the relative contributions of single and multiple scattering in the calculation of the ARF for spherical particles in a viscous medium, as a function of the ultrasound DSA process parameters, including particle size, material properties, and medium viscosity.

We first consider a theoretical case with three spherical particles in a viscous medium and derive operating maps that quantify the deviation between the ARF based on single and multiple scattering as a function of the ultrasound DSA process parameters. Then, we consider a realistic system with hundreds of particles dispersed in a viscous medium relevant to, e.g., manufacturing engineered materials.

Figures 1(a)–(c) illustrate the theoretical model of a three-particle system to simulate the ARF accounting for both single F_{single} and multiple scattering F_{multiple}. Figure 1(a) shows a rectangular reservoir (gray) with two ultrasound transducers on opposing walls (orange) that establish a standing ultrasound wave within the viscous medium contained in the reservoir.

We simulate the incident velocity potential of a plane standing ultrasound wave as $\varphi_{inc}(\mathbf{r}) = e^{i\tilde{k}(x-L/2)} + e^{i\tilde{k}(-x+L/2)}$ inside the reservoir.[50] The color contours in Fig. 1(a) show the magnitude of the incident velocity potential $\Re\{\varphi_{inc}\}$. The distance between both ultrasound transducers $L = 20\lambda$, $\tilde{k} = (\omega/c_m)/(1 - i\omega\tau_s)^{1/2}$ is the complex wave number that accounts for acoustic attenuation in the viscous medium with τ_s the viscous dissipation time to dampen the acoustic pressure to $1/e$ of its original value,[51] c_m is the sound propagation velocity of the medium, ω is the angular frequency, and λ is the wavelength. The incident wave velocity $\mathbf{v}_{inc}(\mathbf{r}) = \nabla\varphi_{inc}(\mathbf{r})$.

Figure 1(b) schematically illustrates single and multiple scattering between three particles. We calculate the ARF at the location of the first particle, which we refer to as the probe particle (maroon). We methodically position the second (orange) and third (gray) particles between a single node and an antinode of the standing ultrasound wave and calculate the ARF at the probe particle. Vectors $\mathbf{r}_1$, $\mathbf{r}_2$, and $\mathbf{r}_3$ describe the locations of the three particles with respect to the origin of the coordinate system in the simulation domain. Using single scattering, the incident wave scatters off the second and third particles once, and these scattered waves superimpose on the incident wave at the probe particle [teal arrows in Fig. 1(b)]. In contrast, considering multiple scattering, the incident wave scatters multiple times between the three particles, and multiple scattered waves superimpose on the incident wave at the probe particle [both teal and gray arrows in Fig. 1(b)].

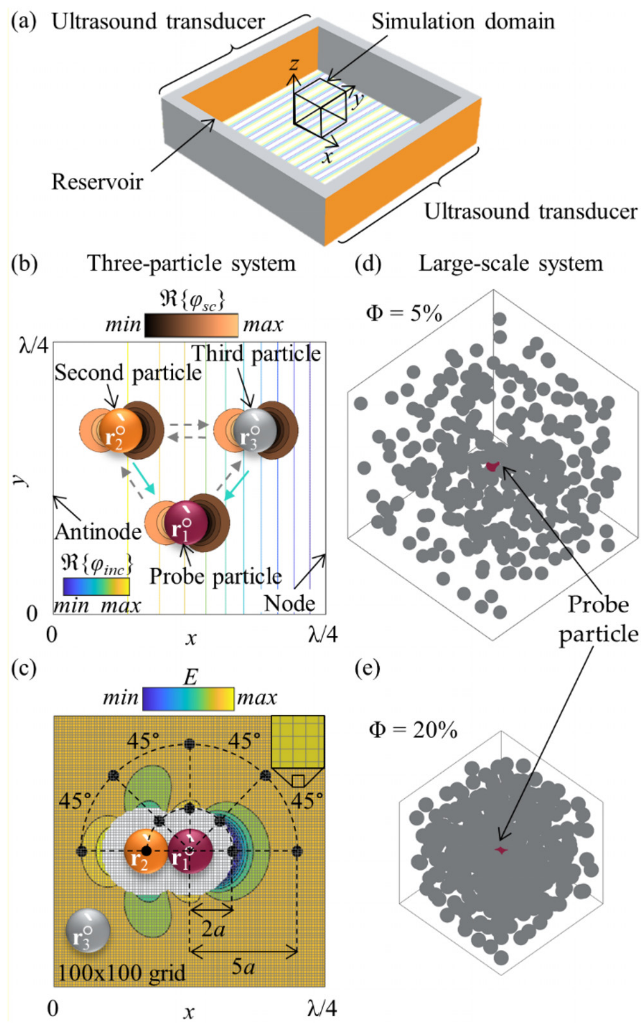

FIG. 1. (a) Schematic of a reservoir (gray) with two ultrasound transducers (orange) and the magnitude of the incident velocity potential φ_{inc} (color contours) of the incident standing ultrasound wave; (b) three-particle system, showing single (teal arrows) and multiple (teal and gray arrows) scattering, superimposed on the incident velocity potential φ_{inc} (color contours) between a single node and antinode; (c) locations of the probe (first) particle, as well as the second and third particle, identifying the exclusion area for the third particle (white area); and (d) large-scale system with $\Phi = 5\%$ and (e) $\Phi = 20\%$.

We express the velocity potential of the ultrasound wave φ_{sc} that scatters off the jth particle located at $\mathbf{r}_j$ and measured at the ith particle located at $\mathbf{r}_i$, accounting for both monopole [first term in Eq. (1)] and dipole [second term in Eq. (1)] scattering as follows:[52,53]

13 May 2024 21:11:51

Published under an exclusive license by AIP Publishing

$$\varphi_{sc}(\mathbf{r}_i,\mathbf{r}_j) = \sigma\varphi(\mathbf{r}_j)G(\mathbf{r}_i,\mathbf{r}_j) + (\mathbf{P}\mathbf{v}(\mathbf{r}_j)).\frac{1}{k^2}\nabla G(\mathbf{r}_i,\mathbf{r}_j). \quad (1)$$

Here, $\varphi(\mathbf{r}_j)$ and $\mathbf{v}(\mathbf{r}_j) = \nabla\varphi(\mathbf{r}_j)$ are the velocity potential and wave velocity at location $\mathbf{r}_j$, respectively, both of which derive from the Helmholtz equation that describes the ultrasound wave within the simulation domain. $G(\mathbf{r}_i,\mathbf{r}_j) = e^{ik|\mathbf{r}_i-\mathbf{r}_j|}/(4\pi|\mathbf{r}_i-\mathbf{r}_j|)$ is the Green's function for the Helmholtz equation in 3D,[54] which relates the ultrasound wave at the particles and within the simulation domain. $\nabla G(\mathbf{r}_i,\mathbf{r}_j)$ is the gradient of the Green's function, and $k = \Re\{\tilde{k}\}$ because viscous attenuation of the ultrasound wave is small ($\approx 0.08\%$) over a short distance between a single node and antinode considered in this work. $\sigma = 4\pi f_1 k^2 a^3/3$ and $\mathbf{P} = -2\pi f_2 k^2 a^3 \mathbf{I}_{3\times3}$ are functions of the monopole f_1 and dipole f_2 scattering coefficients,[55] respectively, where a is the particle radius, and $\mathbf{I}_{3\times3}$ is a three-by-three identity matrix. The monopole scattering coefficient f_1 is a function of the compressibility ratio β_p/β_m, and the dipole scattering coefficient f_2 is a function of the density ratio ρ_p/ρ_m and medium viscosity η_m, where β and ρ are compressibilty and density, and subscripts p and m refer to the particle and fluid medium.[55] Figure 1(b) is a visualization of the magnitude of the monopole and dipole scattering velocity potentials $\Re\{\varphi_{sc}\}$ for all particles (solid copper-color contour plots).

Thus, when considering multiple scattering, the total velocity potential $\varphi(\mathbf{r}_i)$ at location $\mathbf{r}_i$ is the superposition of the incident velocity potential $\varphi_{inc}(\mathbf{r}_i)$ and the sum of the velocity potentials φ_{sc} that result from the scattered ultrasound waves from all other particles, also at $\mathbf{r}_i$, i.e.,

$$\varphi(\mathbf{r}_i) = \varphi_{inc}(\mathbf{r}_i) + \sum_{\substack{j=1\\ j\neq i}}^{N} \varphi_{sc}(\mathbf{r}_i,\mathbf{r}_j). \quad (2)$$

$N = 3$ is the number of particles. Combining Eqs. (1) and (2) yields

$$\varphi(\mathbf{r}_i) = \varphi_{inc}(\mathbf{r}_i) + \sum_{\substack{j=1\\ j\neq i}}^{N}\left[\sigma\varphi(\mathbf{r}_j)G(\mathbf{r}_i,\mathbf{r}_j) + (\mathbf{P}\mathbf{v}(\mathbf{r}_j)).\frac{1}{k^2}\nabla G(\mathbf{r}_i,\mathbf{r}_j)\right]. \quad (3)$$

Furthermore, $\mathbf{v}(\mathbf{r}_i) = \nabla\varphi(\mathbf{r}_i)$, i.e.,

$$\mathbf{v}(\mathbf{r}_i) = \mathbf{v}_{inc}(\mathbf{r}_i) + \sum_{\substack{j=1\\ j\neq i}}^{N}\left[\sigma\varphi(\mathbf{r}_j)\nabla G(\mathbf{r}_i,\mathbf{r}_j) + \frac{1}{k^2}\nabla^2 G(\mathbf{r}_i,\mathbf{r}_j)\mathbf{P}\mathbf{v}(\mathbf{r}_j)\right], \quad (4)$$

where $\nabla^2 G(\mathbf{r}_i,\mathbf{r}_j)$ is the Hessian of the Green's function.[56] We show the linear systems to calculate $\varphi(\mathbf{r}_i)$ [Eq. (3)] and $\mathbf{v}(\mathbf{r}_i)$ [Eq. (4)] in the supplementary material. The ARP at the location of the probe particle $\mathbf{r}_1$ is[55]

$$U(\mathbf{r}_1) = \frac{4\pi}{3}a^3\left(f_1\frac{\beta_m}{2}\langle(i\rho_m\omega\varphi(\mathbf{r}_1))^2\rangle - f_2\frac{3\rho_m}{4}\langle v_x(\mathbf{r}_1)^2\rangle\right), \quad (5)$$

where $v_x(\mathbf{r}_1)$ is the x-component of $\mathbf{v}(\mathbf{r}_1)$ and operator $\langle\cdot\rangle$ averages over a single wave period. The ARF with multiple scattering $F_{\text{multiple}} = -\partial U(\mathbf{r}_1)/\partial x$, using $\varphi(\mathbf{r}_1)$ and $\mathbf{v}(\mathbf{r}_1)$ from Eq.(S1), and the ARF with single scattering $F_{\text{single}} = -\partial U(\mathbf{r}_1)/\partial x$, using $\varphi(\mathbf{r}_1)$ and $\mathbf{v}(\mathbf{r}_1)$ from Eq. (S5). In addition, the PARF $F_{inc} = -\partial U(\mathbf{r}_1)/\partial x$, using $\varphi_{inc}(\mathbf{r}_1)$ and $v_{inc,x}(\mathbf{r}_1)$ in Eq. (5), where $v_{inc,x}(\mathbf{r}_1)$ is the x-component of the incident velocity vector $\mathbf{v}_{inc}(\mathbf{r}_1)$. Additionally, $v_{inc,y}(\mathbf{r}_1) = v_{inc,z}(\mathbf{r}_1) = 0$ for a plane standing ultrasound wave. The percent deviation between the ARF from single and multiple scattering, relative to the PARF is $E = |F_{\text{multiple}} - F_{\text{single}}/F_{inc}|$. We validate our calculation of the AIF based on single and multiple scattering with the experimental results of Mohapatra *et al.*,[30] who measured the AIF between pairs of spherical polystyrene particles in a standing ultrasound wave in water, based on the respective speeds with which they approach each other (see supplementary material).

Figure 1(c) illustrates the possible configurations of the probe, second, and third particles for which we evaluate E. We fix the probe particle at $x = \lambda/8$, i.e., the middle between a node and antinode (white hollow marker), select ten locations for the second particle (black solid marker), and 100×100 locations of the third particle (silver grid, see magnified inset image). We select the ten locations of the second particle based on symmetry. Five of these locations involve contact between the probe and the second particle, whereas the other five locations allow for the third particle to lie between the probe and the second particle. Figure 1(c) illustrates a typical result of E (solid color contour plot) for a single configuration of probe and second particles, and for 100×100 locations of the third particle. The white area around the probe and second particles in Fig. 1(c) is the exclusion area that the third particle center cannot occupy to avoid overlap.

We determine the maximum deviation $E_{\max} = \max(E)$ as a function of ultrasound DSA process parameters and material properties, including the particle size a, the medium viscosity η_m, medium and particle density ρ_m and ρ_p, and medium and particle compressibility β_m and β_p. According to the Buckingham π theorem,[57] four nondimensional parameters are required to describe this system: (i) the nondimensional particle size $0.05 \le K_1 = ka \le 0.20$, which we select to satisfy the Rayleigh regime assumption ($ka \ll 1$), (ii) the nondimensional medium viscosity $0.00 < K_2 = \eta_m/\rho_m\lambda c_m \le 0.27$ that spans the viscosity range of different fluid media previously used with ultrasound DSA in the context of manufacturing engineered materials (e.g., water, photopolymer resin) $0 < \eta_m \le 400$ mPa s,[37] (iii) the density ratio $0 \le \rho_p/\rho_m \le 2.5$, and (iv) the compressibility ratio $0 \le \beta_p/\beta_m \le 2.5$ that spans the density and compressibility ratios of relevant combinations of particles and media for manufacturing engineered materials.[55]

Figures 1(a), 1(c), and 1(d) illustrate the theoretical model of a large-scale system to simulate the ARF accounting for both single F_{single} and multiple scattering F_{multiple}, considering hundreds of randomly dispersed particles in a viscous medium. We illustrate the model with particle volume fraction $\Phi = 5\%$ [Fig. 1(d)] and $\Phi = 20\%$ [Fig. 1(e)]. We fixate the probe particle at $x = \lambda/8$ (maroon particle) and randomly disperse $N = 320$ particles in the solution domain, which we scale to satisfy a specific particle volume fraction $5\% \le \Phi \le 20\%$. We compute the percent deviation E between the ARF for single and multiple scattering, and we measure the distance d between the probe particle and its closest neighbor. For each value of Φ, we perform 250 repeat simulations to quantify the variability of E as a result of the random positions of the particles that affects d.

Figure 2 shows the ratio of the ARFs that account for scattering and the incident ultrasound wave, for (a) single $F_{\text{single}}/F_{inc}$ and (b) multiple scattering $F_{\text{multiple}}/F_{inc}$ in the three-particle system, and

13 May 2024 21:11:51

Published under an exclusive license by AIP Publishing

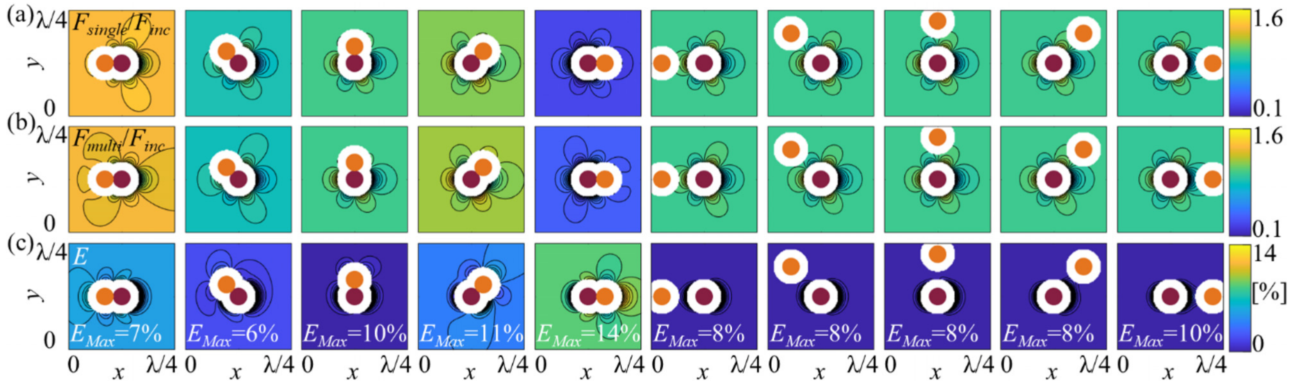

FIG. 2. (a) Single scattering ratio $F_{\text{single}}/F_{inc}$, (b) multiple scattering ratio $F_{\text{multiple}}/F_{inc}$, and (c) the deviation E and E_{Max} for ten locations of the second particle (orange) with respect to the probe particle (maroon) and 100×100 locations of the third particle (not shown), and for $K_1 = 1.2$, $K_2 = 0.14$, $\rho_p/\rho_m = 2.4$, and $\beta_p/\beta_m = 0.029$.

(c) the deviation E between them. Figure 2 shows the results for ten different locations of the second particle relative to the probe particle, and with the third particle at each of the 100×100 grid points. The results are for a single combination of nondimensional parameters:$K_1 = 0.12$, $K_2 = 0.14$, $\rho_p/\rho_m = 2.4$, and $\beta_p/\beta_m = 0.029$, which represent ultrasound DSA of aluminum spherical particles ($a = 19$ μm, $\rho_p = 2700$ kg/m^3, and $\beta_p = 1.3 \times 10^{-11}$ Pa^{-1})[54] in photopolymer resin ($\eta_m = 200$ mPa s, $\rho_m = 1110$ kg/m^3, and $\beta_m = 4.5 \times 10^{-10}$ Pa^{-1})[37] with $k = 6.64 \times 10^3$.

The relative locations of the three particles determine $F_{\text{single}}/F_{inc}$, $F_{\text{multiple}}/F_{inc}$, and E, which depend on both monopole and dipole scattering [$G(\mathbf{r}_n, \mathbf{r}_j)$ and $\nabla G(\mathbf{r}_n, \mathbf{r}_j)$ in Eq. (3)]. Furthermore, the angle between their lines of centers and the wave propagation direction (x-direction) affects the dipole scattering coefficient. Generally, maximum values of $F_{\text{single}}/F_{inc}$, $F_{\text{multiple}}/F_{inc}$, and E_{Max} occur where particles contact each other in the wave propagation direction because dipole scattering is maximum in that configuration.

Figure 3 shows the maximum percent deviation E_{Max} between the ARF based on single and multiple scattering, (a) as a function of nondimensional particle size K_1 and nondimensional medium viscosity K_2 for $\rho_p/\rho_m = 2.4$ and $\beta_p/\beta_m = 0.029$, (b) as a function of density ratio ρ_p/ρ_m and compressibility ratio β_p/β_m for $K_1 = 1.2$, and $K_2 = 0.14$, where the particle is denser and less compressible than the fluid medium ($\rho_p/\rho_m \geq 1$ and $\beta_p/\beta_m \leq 1$), and (c) as a function of density ratio ρ_p/ρ_m and compressibility ratio β_p/β_m for $K_1 = 1.2$, and $K_2 = 0.14$, where the particle is less dense and more compressible than the fluid medium ($\rho_p/\rho_m \leq 1$ and $\beta_p/\beta_m \geq 1$).

We observe that $E_{\max}$ increases with decreasing K_1 and increasing K_2. Decreasing K_1 decreases the distance between neighboring particles, which increases the dipole scattering term in Eq. (1) that affects both single and multiple scattering and, thus, increases $E_{\max}$. Furthermore, $E_{\max}$ increases with increasing ρ_p/ρ_m and increasing β_p/β_m. First, in the Rayleigh regime ($ka \ll 1$), dipole dominates monopole scattering because the gradient of the Green's function $k^{-1}\nabla G(\mathbf{r}_i, \mathbf{r}_j)$ in the x-direction is larger than the Green's function $G(\mathbf{r}_i, \mathbf{r}_j)$ itself [see Eq. (1)]. Second, maximum scattering between particles occurs when their line of centers is parallel to the wave propagation direction where $k^{-1}\nabla G(\mathbf{r}_i, \mathbf{r}_j)$ is maximum. Under these

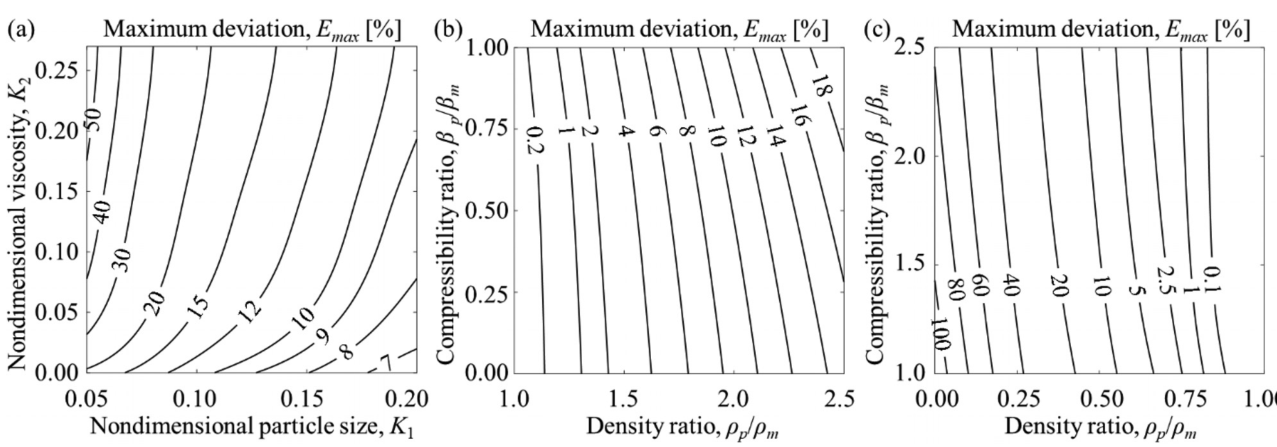

FIG. 3. Deviation E_{Max} between the ARF based on single and multiple scattering (a) as a function of K_1 and K_2 for $\rho_p/\rho_m = 2.4$ and $\beta_p/\beta_m = 0.029$, and (b) and (c) as a function of ρ_p/ρ_m and β_p/β_m for $K_1 = 1.2$, and $K_2 = 0.14$.

13 May 2024 21:11:51

Published under an exclusive license by AIP Publishing

circumstances, dipole scattering causes particles to repel, whereas monopole scattering causes particles to attract each other. Thus, monopole scattering and dipole scattering counteract each other in the x-direction, where the effect of dipole scattering is dominant. As a result, increasing ρ_p/ρ_m and β_p/β_m increases the dipole scattering coefficient f_2 and decreases the monopole scattering coefficient f_1. Since the scattering coefficients affect both single and multiple scattering, it increases $F_{\text{single}}/F_{inc}$ and $F_{\text{multiple}}/F_{inc}$ and, thus, E_{Max}. The results show that $E_{\max}$ can reach up to 100%, which contrasts previous works in the literature concluding that multiple scattering is negligible compared to single scattering in the calculation of the AIF and ARF.[26,28,29,31] However, these works focus on systems with two rather than three (or many) particles, which cannot entirely describe the effect of multiple scattering.

Figure 4(a) shows the percent deviation E vs the shortest distance between neighboring particles d for 250 different configurations of 320 randomly dispersed particles around the probe particle, for four different particle volume fractions $\Phi = 5\%$, 10%, 15%, and 20%, and for $K_1 = 0.05$, $K_2 = 0.27$, $\rho_p/\rho_m = 2.4$, and $\beta_p/\beta_m = 0.029$. We use transparent solid data points so that increasing darkness signifies an increasing number of overlapping data points. The data shows that decreasing the distance d between the probe particle and its nearest neighbor increases the deviation E, independent of Φ, because the distance between particles is one of the main parameters that drives the relative importance between monopole and dipole scattering (Fig. 2). Additionally, Fig. 4(b) shows the probability density function of E, and its mean value E_{mean} for 250 configurations of 320 randomly dispersed particles around the probe particle, for the results of Fig. 4(a). The likelihood of a small distance $d \approx 2a$ increases with increasing Φ because it increases the number of non-overlapping particles in the solution domain. Thus, multiple scattering becomes increasingly important with increasing Φ because the interactions between particles increase.

This methodical study highlights the importance of considering multiple scattering effects in ultrasound DSA simulations under certain conditions; the operating maps of Fig. 3 guide the choice between both scattering approaches in ultrasound DSA simulations. However, limitations still exist. We simulate the incident wave as a perfect plane standing wave, but realistic transducers cannot generate a perfect wave, and reflections from the near-field interfere with the reservoir walls and potentially affect the results. Furthermore, the medium viscosity may induce nonlinear phenomena such as streaming at the reservoir walls and microstreaming around the particles, which could affect the ARF.[58,59] In practice, imperfect dispersion, shape, and size of the spherical particles as well as thermal fluctuations in the viscous medium[60] also affect the ARF.

We conclude that the deviation E between the ARF derived from single and multiple scattering may reach up to 100%, depending on the ultrasound DSA process parameters and material properties. Thus, neglecting multiple scattering in favor of computationally efficient single scattering is not always correct. Physically, the distance between spherical particles, the angle between their lines of centers relative to the wave propagation direction, the ultrasound DSA process parameters (nondimensional particle size K_1, nondimensional viscosity K_2, particle volume fraction Φ), and the material properties (density ratio ρ_p/ρ_m and compressibility ratio β_p/β_m) determine the relative magnitude of monopole and dipole scattering between spherical particles in a standing ultrasound wave and, thus, E. The maximum deviation $E_{\max}$ occurs when particles contact each other in the wave propagation direction because this configuration causes the largest dipole scattering between particles. Furthermore, E increases with decreasing K_1 and increasing K_2, and with ρ_p/ρ_m and increasing ratio β_p/β_m, largely driven by increasing dipole scattering that affects both single and multiple scattering and, thus, increases E. Comparing the fundamental three-particle system to a large-scale system shows that increasing Φ increases E because it increases the number of particles in a constant

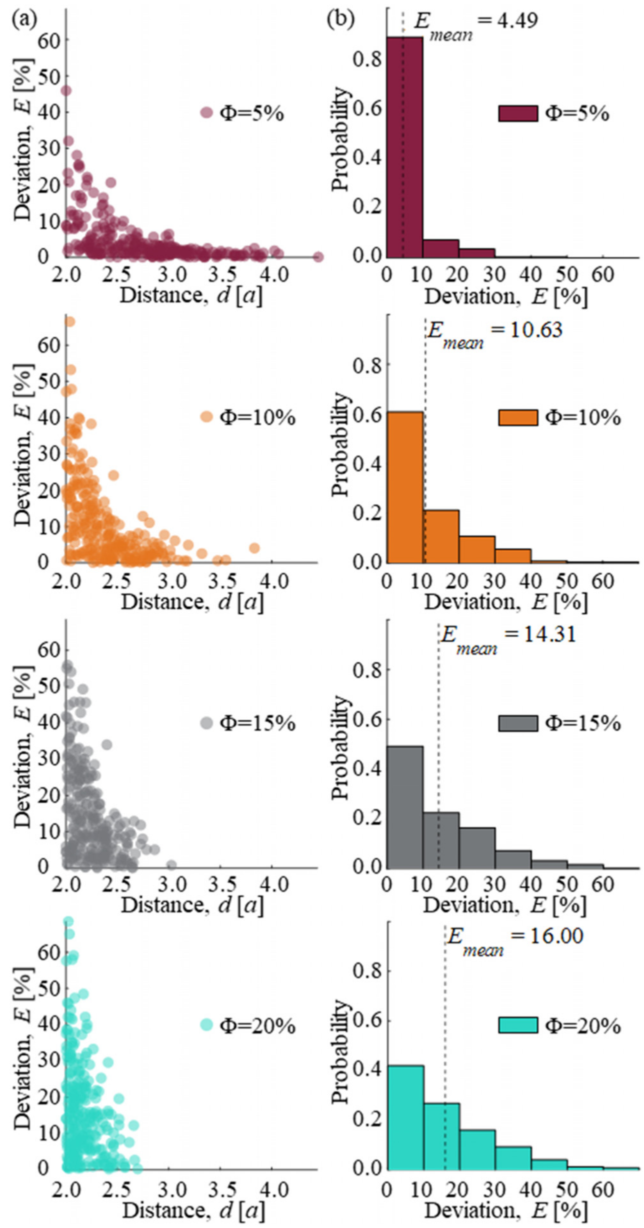

FIG. 4. (a) Deviation E as a function of d and (b) probability density function of E, for $\Phi = 5\%$, 10%, 15%, and 20%, and for $K_1 = 0.05$, $K_2 = 0.27$, $\rho_p/\rho_m = 2.4$, and $\beta_p/\beta_m = 0.029$.

13 May 2024 21:11:51

Published under an exclusive license by AIP Publishing

control volume, decreases the distance between them, and increases both single and multiple scattering.

See the supplementary material shows the derivation of Eqs. (3) and (4) and illustrates experimental validation of the model.

S.N., M.F., and B.R. acknowledge the support of the National Science Foundation under Award No. CMMI-2130083. F.G.V. acknowledges the support of the National Science Foundation under Award Nos. DMS-2008610 and DMS-2136198.

AUTHOR DECLARATIONS

Conflict of Interest

The authors have no conflicts to disclose.

Author Contributions

Soheyl Noparast: Conceptualization (equal); Data curation (lead); Formal analysis (lead); Investigation (lead); Methodology (equal); Visualization (lead); Writing – original draft (lead); Writing – review & editing (equal). **Fernando Guevara Vasquez:** Conceptualization (equal); Formal analysis (equal); Investigation (equal); Methodology (equal); Supervision (supporting); Visualization (equal); Writing – original draft (equal); Writing – review & editing (equal). **Mathieu Francoeur:** Conceptualization (equal); Funding acquisition (equal); Visualization (supporting); Writing – review & editing (supporting). **Bart Raeymaekers:** Conceptualization (lead); Formal analysis (equal); Funding acquisition (equal); Methodology (equal); Project administration (lead); Supervision (lead); Visualization (supporting); Writing – original draft (equal); Writing – review & editing (lead).

DATA AVAILABILITY

The data that support the findings of this study are available from the corresponding author upon reasonable request.

REFERENCES

[1] L. P. Gor'kov, "On the forces acting on a small particle in an acoustical field in an ideal fluid," Sov. Phys. Dokl. **6**, 773 (1962).
[2] S. Noparast, F. Guevara Vasquez, and B. Raeymaekers, "The effect of medium viscosity and particle volume fraction on ultrasound directed self-assembly of spherical microparticles," J. Appl. Phys. **131**(13), 134901 (2022).
[3] T. Schwarz, G. Petit-Pierre, and J. Dual, "Rotation of non-spherical microparticles by amplitude modulation of superimposed orthogonal ultrasonic modes," J. Acoust. Soc. Am. **133**(3), 1260–1268 (2013).
[4] X. Chen and R. E. Apfel, "Radiation force on a spherical object in an axisymmetric wave field and its application to the calibration of high-frequency transducers," J. Acoust. Soc. Am. **99**(2), 713–724 (1996).
[5] A. Haake, A. Neild, D.-H. Kim, J.-E. Ihm, Y. Sun, J. Dual, and B.-K. Ju, "Manipulation of cells using an ultrasonic pressure field," Ultrasound Med. Biol. **31**(6), 857–864 (2005).
[6] A. L. Bernassau, C. R. P. Courtney, J. Beeley, B. W. Drinkwater, and D. R. S. Cumming, "Interactive manipulation of microparticles in an octagonal sonotweezer," Appl. Phys. Lett. **102**(16), 164101 (2013).
[7] C. R. P. Courtney, C. E. M. Demore, H. Wu, A. Grinenko, P. D. Wilcox, S. Cochran, and B. W. Drinkwater, "Independent trapping and manipulation of microparticles using dexterous acoustic tweezers," Appl. Phys. Lett. **104**(15), 154103 (2014).
[8] A. Marzo, S. A. Seah, B. W. Drinkwater, D. R. Sahoo, B. Long, and S. Subramanian, "Holographic acoustic elements for manipulation of levitated objects," Nat. Commun. **6**(1), 8661 (2015).
[9] R. Hirayama, D. Martinez Plasencia, N. Masuda, and S. Subramanian, "A volumetric display for visual, tactile and audio presentation using acoustic trapping," Nature **575**(7782), 320–323 (2019).
[10] T. Fushimi, A. Marzo, B. W. Drinkwater, and T. L. Hill, "Acoustophoretic volumetric displays using a fast-moving levitated particle," Appl. Phys. Lett. **115**(6), 064101 (2019).
[11] M. Wu, A. Ozcelik, J. Rufo, Z. Wang, R. Fang, and T. Jun Huang, "Acoustofluidic separation of cells and particles," Microsyst. Nanoeng. **5**(1), 1–18 (2019).
[12] E. V. Skorb, H. Möhwald, T. Irrgang, A. Fery, and D. V. Andreeva, "Ultrasound-assisted design of metal nanocomposites," Chem. Commun. **46**(42), 7897–7899 (2010).
[13] M. D. Haslam and B. Raeymaekers, "Aligning carbon nanotubes using bulk acoustic waves to reinforce polymer composites," Composites, Part B **60**, 91–97 (2014).
[14] J. Greenhall, L. Homel, and B. Raeymaekers, "Ultrasound directed self-assembly processing of nanocomposite materials with ultra-high carbon nanotube weight fraction," J. Compos. Mater. **53**(10), 1329–1336 (2019).
[15] T. A. Ogden, M. Prisbrey, I. Nelson, B. Raeymaekers, and S. E. Naleway, "Ultrasound freeze casting: Fabricating bioinspired porous scaffolds through combining freeze casting and ultrasound directed self-assembly," Mater. Des. **164**, 107561 (2019).
[16] M. Mroz, J. L. Rosenberg, C. Acevedo, J. J. Kruzic, B. Raeymaekers, and S. E. Naleway, "Ultrasound freeze-casting of a biomimetic layered microstructure in epoxy-ceramic composite materials to increase strength and hardness," Materialia **12**, 100754 (2020).
[17] R. R. Collino, T. R. Ray, R. C. Fleming, C. H. Sasaki, H. Haj-Hariri, and M. R. Begley, "Acoustic field controlled patterning and assembly of anisotropic particles," Extreme Mech. Lett. **5**, 37–46 (2015).
[18] L. Friedrich, R. Collino, T. Ray, and M. Begley, "Acoustic control of microstructures during direct ink writing of two-phase materials," Sens. Actuators, A **268**, 213–221 (2017).
[19] P. Wadsworth, I. Nelson, D. L. Porter, B. Raeymaekers, and S. E. Naleway, "Manufacturing bioinspired flexible materials using ultrasound directed self-assembly and 3D printing," Mater. Des. **185**, 108243 (2020).
[20] A. Felt and B. Raeymaekers, "Ultrasound directed self-assembly of filler in continuous flow of a viscous medium through an extruder nozzle for additive manufacturing," Addit. Manuf. Lett. **5**, 100120 (2023).
[21] J. Greenhall and B. Raeymaekers, "3D printing macroscale engineered materials using ultrasound directed self-assembly and stereolithography," Adv. Mater. Technol. **2**(9), 1700122 (2017).
[22] D. E. Yunus, S. Sohrabi, R. He, W. Shi, and Y. Liu, "Acoustic patterning for 3D embedded electrically conductive wire in stereolithography," J. Micromech. Microeng. **27**(4), 045016 (2017).
[23] T. M. Llewellyn-Jones, B. W. Drinkwater, and R. S. Trask, "3D printed components with ultrasonically arranged microscale structure," Smart Mater. Struct. **25**(2), 02LT01 (2016).
[24] S. Noparast, F. Guevara Vasquez, M. Francoeur, and B. Raeymaekers, "Measuring and simulating the transient packing density during ultrasound directed self-assembly and vat polymerization manufacturing of engineered materials," Adv. Mater. Technol. 2301950 (2024).
[25] L. Lu, Z. Zhang, J. Xu, and Y. Pan, "3D-printed polymer composites with acoustically assembled multidimensional filler networks for accelerated heat dissipation," Composites, Part B **174**, 106991 (2019).
[26] G. T. Silva and H. Bruus, "Acoustic interaction forces between small particles in an ideal fluid," Phys. Rev. E **90**(6), 063007 (2014).
[27] S. Sepehrirahnama, K.-M. Lim, and F. S. Chau, "Numerical study of interparticle radiation force acting on rigid spheres in a standing wave," J. Acoust. Soc. Am. **137**(5), 2614–2622 (2015).
[28] T. Baasch, I. Leibacher, and J. Dual, "Multibody dynamics in acoustophoresis," J. Acoust. Soc. Am. **141**(3), 1664–1674 (2017).
[29] S. Zhang, C. Qiu, M. Wang, M. Ke, and Z. Liu, "Acoustically mediated long-range interaction among multiple spherical particles exposed to a plane standing wave," New J. Phys. **18**(11), 113034 (2016).
[30] A. R. Mohapatra, S. Sepehrirahnama, and K.-M. Lim, "Experimental measurement of interparticle acoustic radiation force in the Rayleigh limit," Phys. Rev. E **97**(5), 053105 (2018).

13 May 2024 21:11:51

Published under an exclusive license by AIP Publishing

[31] S. Sepehrirhnama and K.-M. Lim, "Generalized potential theory for close-range acoustic interactions in the Rayleigh limit," Phys. Rev. E **102**(4), 043307 (2020).
[32] M. Azarpeyvand, M. Alibakhshi, and R. Self, "Effects of multi-scattering on the performance of a single-beam acoustic manipulation device," IEEE Trans. Ultrason., Ferroelectr., Freq. Control **59**(8), 1741–1749 (2012).
[33] A. A. Doinikov, "Acoustic radiation interparticle forces in a compressible fluid," J. Fluid Mech. **444**, 1–21 (2001).
[34] J. H. Lopes, M. Azarpeyvand, and G. T. Silva, "Acoustic interaction forces and torques acting on suspended spheres in an ideal fluid," IEEE Trans. Ultrason., Ferroelectr., Freq. Control **63**(1), 186–197 (2016).
[35] X. Zheng and R. E. Apfel, "Acoustic interaction forces between two fluid spheres in an acoustic field," J. Acoust. Soc. Am. **97**(4), 2218–2226 (1995).
[36] S. Sepehrirahnama, F. S. Chau, and K.-M. Lim, "Effects of viscosity and acoustic streaming on the interparticle radiation force between rigid spheres in a standing wave," Phys. Rev. E **93**(2), 023307 (2016).
[37] S. Noparast, F. Guevara Vasquez, M. Francoeur, and B. Raeymaekers, "Measuring and simulating the local packing density resulting from ultrasound-directed self-assembly of spherical microparticles into specific patterns," Phys. Rev. Appl. **19**(6), 064087 (2023).
[38] J. Greenhall, F. Guevara Vasquez, and B. Raeymaekers, "Continuous and unconstrained manipulation of micro-particles using phase-control of bulk acoustic waves," Appl. Phys. Lett. **103**(7), 074103 (2013).
[39] A. Grinenko, P. D. Wilcox, C. R. P. Courtney, and B. W. Drinkwater, "Proof of principle study of ultrasonic particle manipulation by a circular array device," Proc. R Soc. A **468**(2147), 3571–3586 (2012).
[40] J. Greenhall, F. Guevara Vasquez, and B. Raeymaekers, "Ultrasound directed self-assembly of user-specified patterns of nanoparticles dispersed in a fluid medium," Appl. Phys. Lett. **108**(10), 103103 (2016).
[41] E. Cherkaev, F. Guevara Vasquez, C. Mauck, M. Prisbrey, and B. Raeymaekers, "Wave-driven assembly of quasiperiodic patterns of particles," Phys. Rev. Lett. **126**(14), 145501 (2021).
[42] Y. Ochiai, T. Hoshi, and J. Rekimoto, "Three-dimensional mid-air acoustic manipulation by ultrasonic phased arrays," PLoS One **9**(5), e97590 (2014).
[43] M. Prisbrey, J. Greenhall, F. Guevara Vasquez, and B. Raeymaekers, "Ultrasound directed self-assembly of three-dimensional user-specified patterns of particles in a fluid medium," J. Appl. Phys. **121**(1), 014302 (2017).
[44] T. Hoshi, Y. Ochiai, and J. Rekimoto, "Three-dimensional noncontact manipulation by opposite ultrasonic phased arrays," Jpn. J. Appl. Phys., Part 1 **53**(7S), 07KE07 (2014).
[45] K. Niendorf and B. Raeymaekers, "Quantifying macro- and microscale alignment of carbon microfibers in polymer-matrix composite materials fabricated using ultrasound directed self-assembly and 3D-printing," Compos. Part Appl. Sci. Manuf. **129**, 105713 (2020).
[46] M. Prisbrey and B. Raeymaekers, "Aligning high-aspect-ratio particles in user-specified orientations with ultrasound-directed self-assembly," Phys. Rev. Appl. **12**(1), 014014 (2019).
[47] M.-S. Scholz, B. W. Drinkwater, and R. S. Trask, "Ultrasonic assembly of anisotropic short fibre reinforced composites," Ultrasonics **54**(4), 1015–1019 (2014).
[48] M. Prisbrey and B. Raeymaekers, "Ultrasound noncontact particle manipulation of three-dimensional dynamic user-specified patterns of particles in air," Phys. Rev. Appl. **10**(3), 034066 (2018).
[49] M. Prisbrey, F. Guevara Vasquez, and B. Raeymaekers, "Arranging ellipsoidal particles in three-dimensional user-specified orientations with ultrasound-directed self-assembly," Phys. Rev. Appl. **14**(2), 024026 (2020).
[50] J. Greenhall, F. G. Vasquez, and B. Raeymaekers, "Dynamic behavior of microscale particles controlled by standing bulk acoustic waves," Appl. Phys. Lett. **105**(14), 144105 (2014).
[51] L. E. Kinsler, A. R. Frey, A. B. Coppens, and J. V. Sanders, *Fundamental of Acoustic*, 4th ed. (John Wiley & Sons, Inc., New York, 2000).
[52] K. Huang, K. Solna, and H. Zhao, "Generalized Foldy-Lax formulation," J. Comput. Phys. **229**(12), 4544–4553 (2010).
[53] P. A. Martin, *Multiple Scattering: Interaction of Time-Harmonic Waves with N Obstacles* (Cambridge University Press, Cambridge, 2006).
[54] W. M. Haynes, D. R. Lide, and T. J. Bruno, *CRC Handbook of Chemistry and Physics*, 95th ed. (CRC Press, Boca Raton, 2014).
[55] M. Settnes and H. Bruus, "Forces acting on a small particle in an acoustical field in a viscous fluid," Phys. Rev. E **85**(1), 016327 (2012).
[56] "DLMF: NIST Digital Library of Mathematical Functions," Release 1.2.0 (NIST, 2024), Chap. 10, available at https://dlmf.nist.gov/10.51
[57] L. P. Yarin, *The Pi-Theorem: Applications to Fluid Mechanics and Heat and Mass Transfer* (Springer, Berlin, Heidelberg, 2012).
[58] N. St. Clair, D. Davenport, A. D. Kim, and D. Kleckner, "Dynamics of acoustically bound particles," Phys. Rev. Res. **5**(1), 013051 (2023).
[59] A. Pavlic, L. Ermanni, and J. Dual, "Interparticle attraction along the direction of the pressure gradient in an acoustic standing wave," Phys. Rev. E **105**(5), L053101 (2022).
[60] A. A. Doinikov, "Acoustic radiation force on a spherical particle in a viscous heat-conducting fluid. II. Force on a rigid sphere," J. Acoust. Soc. Am. **101**(2), 722–730 (1997).

13 May 2024 21:11:51

Published under an exclusive license by AIP Publishing